Adaptive mesh refinement and turbulence modeling for vortex interactions : Aero2024-29-Visonneau

M Visonneau, E Guilmineau, P Spalart

Association Aéronautique et Astronautique de France

58th 3AF International Conference on Applied Aerodynamics
27 — 29 March 2024, Orléans – France

AERO2024-29-VISONNEAU

ADAPTIVE MESH REFINEMENT AND TURBULENCE MODELING FOR VORTEX INTERACTIONS

M. Visonneau[(1)], E. Guilmineau[(1)] and P. Spalart[(2)]

[(1)]LHEEA, CNRS UMR 6598, Centrale Nantes, France, michel.visonneau@ec-nantes.fr, emmanuel.guilmineau@ec-nantes.fr

[(2)]Retired from Boeing, Woodinville, USA, prspalart@gmail.com

ABSTRACT

Simulations of the flow over a generic fighter-airplane configuration are presented and analyzed in detail. Grid adaptation is essential to limit the errors, which interfere with physical reasoning, although true grid convergence is still out of reach. Turbulence is treated with two conventional RANS models, one of which is based on the Reynolds stresses (RSTM), and by a hybrid RANS-LES approach called DDES which resolves the turbulence activity, to the extent allowed by the grid, outside the boundary layers. A central difficulty of this fighter triple-delta wing is the axial flow in the various over-wing vortices, which can be of jet-type or wake-type, and switch abruptly along a vortex. The associated pressure changes in some cases reverse the rolling moment on the airplane, at a high angle of attack with side-slip; this is an important design criterion. Comparisons with experimental field measurements are included, and generally favor DDES although it depends on the angles of attack and side-slip, and on which wing is considered. A rigorous post-processing system gives the budget of the Reynolds stresses following leading-edge separation, roll-up of the shear layer, and maturation of the vortices. This system incorporates the time-averaged effects of the sub-grid-scale terms, which appears to be a new and non-trivial step, and the sum of the terms approaches 0, which is not easy to achieve because energy conservation is not exact in simulations. This knowledge is expected to guide future RANS-model improvements, both of the eddy-viscosity and Reynolds-stress type.

1. INTRODUCTION

A critical issue that needs to be addressed in the simulation of flows around modern fighter aircraft is the rolling stability in sideslip conditions. As illustrated by Figure 3, which shows the evolution of the lateral forces and moments at a 5° sideslip angle on the non-proprietary fighter aircraft NA_W1 (configuration shown in Figure 1), a sudden change of behaviour of the rolling moment occurs at an angle of attack of 16°, which leads quickly to a change of sign causing a loss of rolling stability.

The numerical prediction of this change of sign is a formidable challenge for current turbulence models, as it results from the vortex-vortex interaction and the effect of this interaction on the individual vortex core flow regions. The understanding of the physical mechanisms involved and the identification of the best turbulence models was one of the main objectives of the NATO/AVT-316 collaborative research entitled "Vortex Interaction Effects Relevant to Military Air Vehicle Performance", in which the first two authors participated. However, a rigorous assessment of the physical models cannot be performed without controlling the local discretisation error affecting the numerical solution in the core of vortices, which is difficult if not impossible without the help of anisotropic grid adaptation. This paper will report on our progress on this topic, and will try to shed some light on these delicate matters.

2. DESCRIPTION OF THE TEST CASE

Fig. 1 illustrates the test configuration [8, 10]. The so-called NA1_W1 geometry studied in this paper is a triple delta wing configuration with three different consecutive wing sections featuring a varying leading-edge sweep. The inboard and outboard wing sections exhibit a moderate leading-edge sweep of $\varphi_1 = \varphi_3 = 52.5°$ and the mid-board wing section is highly swept at $\varphi_2 = 75.0°$.

Experiments have been conducted in the wind tunnel of the Technical University of Munich (TUM). The model

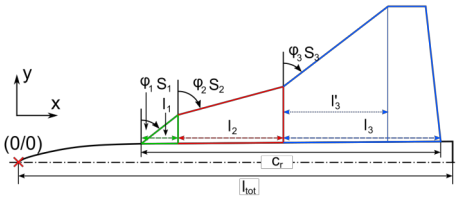

Figure 1: NA1_W1 wing planform.

has a total length of l_{tot} = 1.160 m and a root chord of c_r = 0.802 m; the speed is V_∞ = 51.97 m/s which leads to a Reynolds number, based on c_r, of 2.36 $\times$ 10^6 and a Mach number of 0.15. Two side slip angles, β, were investigated: 0° and 5°.

3. THE NUMERICS

3.1 ISIS-CFD at a glance

The in-house solver ISIS-CFD used in this study and also available as a part of the FINE™/Marine computing suite worldwide distributed by Cadence Design Systems is an incompressible multiphase unsteady Reynolds-averaged Navier-Stokes (URANS) solver mainly devoted to marine hydrodynamics. It is based on a fully-unstructured (face-based) finite volume discretization with specific functionalities needed for multiphase flows and industrial applications. The method features several sophisticated turbulence models: apart from the classical two-equation k-ε and k-ω models, the anisotropic two-equation Explicit Algebraic Reynolds Stress Model (EARSM), as well as Reynolds Stress Transport Models (RSTM), are available, see Deng et al. (1999) [4], Duvigneau & Visonneau (2003) [5] and [2]. All models are available with wall-function or low-Reynolds near wall formulations. Hybrid RANS/LES turbulence models based on Detached Eddy Simulation (DES-SST, DDES-SST, ID-DES) are also implemented and have been thoroughly validated on automotive flows characterized by large separations, see Guilmineau et al. (2015) [7] and ships at steady drift [11]. Moreover, the solver accepts sliding and overset grids and features an anisotropic adaptive grid refinement functionality ([12], [9]) applied to unstructured hexahedral meshes which will be used extensively in this study.

3.2 The anisotropic adaptive mesh refinement

The grids employed in this study are generated with the help of the anisotropic adaptive grid functionality embedded in our flow solver ISIS-CFD, which is an essential element for complex-flow simulation due to the difficulty of creating high-resolution meshes for such flows by hand. The choice of where to refine the grid is handled by the refinement criterion, formulated in the metric context [6, 1]. The criterion is a symmetric 3×3 tensor field computed from the flow, which indicates the optimal local cell sizes in all directions. The actual mesh is then refined to fit this specification as closely as possible. The metric approach is very flexible; in this particular study, we use as refinement criteria the so-called flux-component Hessian based on the second derivatives of the velocity fluxes and pressure.

For all turbulence closures, computations are conducted in an unsteady way and the grid adaptation is based on time-averaged refinement criteria following the methodology described in [9]. For resolved turbulence, mesh refinement is no longer only a means to reduce the numerical error: the mesh resolution and the turbulence/subgrid-scale (SGS) model influence each other and have to be mutually adjusted to obtain optimal results. A finer mesh produces a lower SGS viscosity, which is desirable. Fig. 2 presents the converged flow-adapted grids used for the computations performed around the NA1_W1 airfighter configuration with the k-ω SST and hybrid RANS/LES DDES-SST closures at an angle of attack of 24°. Only the cross-section x/c_r=0.592 is shown in this figure. The global flow-adapted grid for the k-ω SST (resp. DDES-SST) is comprised of 89.6M (resp. 97.9M) cells. In industrial work, the DDES grid would have substantially more points. The typical size of cells inside the core of the main vortex is around 0.69mm, while the model size is about 1m.

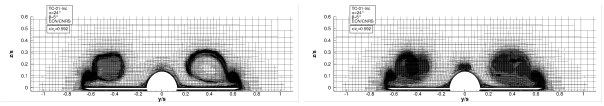

(a) $k-\omega$ SST $\alpha = 24°$, $\beta = 5°$ (b) DDES-SST $\alpha = 24°$, $\beta = 5°$

Figure 2: α = 24°, β = 5°- Views of the flow-adapted grids at the cross-section x/c_r=0.592.

4. THE REVERSAL OF ROLLING MOMENT

4.1 Forces and moments for a side-slip angle β = 5°

Fig. 3 presents the evolution of the lateral force and moment coefficients versus the angle of attack for the configuration NA1_W1. On one hand, the side-slip coefficient C_s and C_{mz} coefficient are accurately predicted by $k-\omega$ SST and DDES-SST, with a slight improvement brought by DDES-SST on C_s for the highest computed angle of attack, α=32°. On the other hand, the numerical prediction of the rolling moment coefficient C_{mx} is very inaccu-

rate for $k-\omega$ SST which is not able to capture the decay and the change of slope occurring around 16°. Hybrid RANS/LES computations look more promising at α=16° with the right negative value and a moderate increase at $\alpha = 18°$ while the rolling moment coefficient should be close to zero, according to the measurements. But for higher angles of attack, i.e. 20° and 24°, the predicted rolling moment coefficient decreases again, instead of keeping close to zero, as indicated in the experiments.
This change of trend between 16°, 18° and 20° needs to be correlated to the local behaviour of the leeward and windward vortices. Of course, the range of variation of the rolling moment being very small, it is hard to simulate accurately and to track the local flow characteristics. For the highest computed angle of attack, 32°, both models are able to accurately predict the high positive value of C_{mx}, as if a sudden change of topology had taken place, removing the incorrect numerical flow configuration predicted in the range of 18° to 24°. This means that the critical change of sign of the rolling moment, which governs the roll stability of the aircraft, is numerically predicted by both turbulence closures at an angle of attack located somewhere between 24° and 32° instead of 16°, as indicated by the experiments.

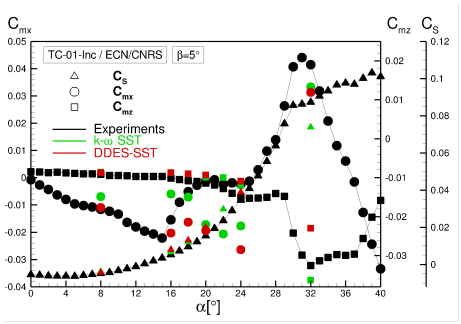

(a) Lateral coefficients

Figure 3: Lateral aerodynamic coefficients for the NA1_W1 configuration for $\beta = 5°$ versus α.

4.2 Local flow analysis and comparison with experiments

4.2.1 Angle of attack α=24°

Figs. 4 and 5 show the vortical structures (identified by the Q criterion and the streamwise velocity), surface pressure distributions and skin friction lines at 24°, which is within the problematic range. DDES-SST predicts more intense vortical structures on both leeward and windward wings, but the surface pressure and skin friction lines remain globally unchanged by the turbulence closures. For this angle of attack a flow reversal, indicated by the red surfaces (some of them hidden), is observed in the IBV (Inboard Vortex) vortex all along its trajectory on the windward wing while flow reversal occurs only close to the trailing edge of the leeward wing and this for both turbulence closures.

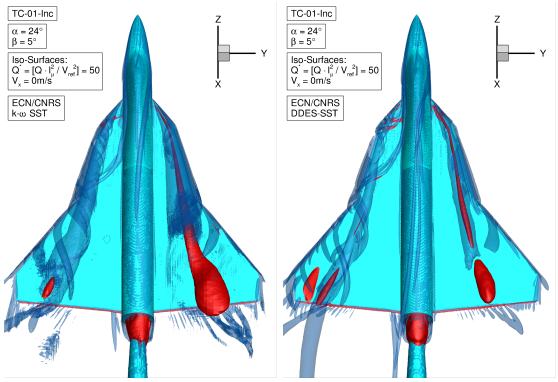

(a) k-ω SST (b) DDES-SST

Figure 4: Time averaged vortical structures for $\alpha = 24°$ and $\beta = 5°$.

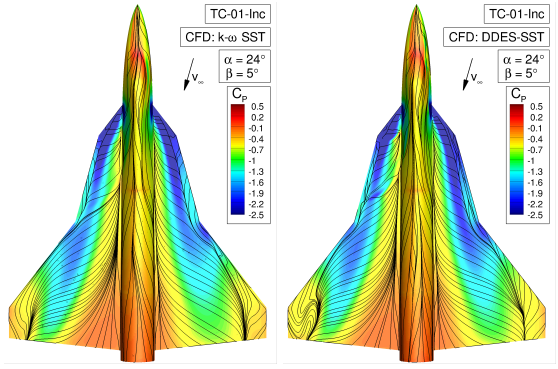

(a) k-ω SST (b) DDES-SST

Figure 5: Surface pressure distribution and skin friction lines for $\alpha = 24°$ and $\beta = 5°$.

Fig. 6 shows the crosswise dimensionless axial velocity component at $x/c_r = 0.592$ for an angle of attack of 24°. In this figure and all similar ones, black lines are contours of pressure, and a pressure minimum is an excellent reference when searching for the center of a vortex. TUM experiments reveal a strong asimmetry of the inner structure of the vortices developing on each wing. On the leeward wing, both the IBV (inboard) and MBV (mid-board) vortices are clearly jet-type vortices with a strong overshoot of axial velocity in the core of both vortices (around 2.5 for IBV and 1.5 for MBV) (see Figs. 6a, 6b and 6c). On the windward wing, the IBV vortex is of wake type with a core axial velocity component close to zero at this section while the MBV vortex keeps its jet-type characteristic. None of the turbulence closures is able to reproduce the correct behaviour in the core of the IBV vortex on the leeward wing, $k-\omega$ SST providing a

very similar longitudinal velocity distribution to that from DDES-SST, in both cases smaller than the measurements at this cross-section. In contrast, on the windward wing both k-ω SST and DDES-SST models are able to capture the strong decrease of the core axial velocity in the IBV vortex.

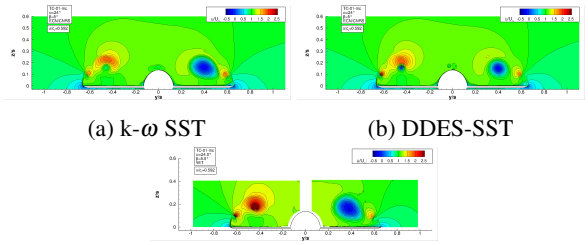

(a) k-ω SST (b) DDES-SST

(c) TUM experiments

Figure 6: Axial component of the velocity at $x/c_r = 0.592$ at $\alpha = 24°$ and $\beta = 5°$.

Fig. 7a (resp. 7b) shows the dimensionless axial velocity, u/U_∞, in the inboard vortex (IBV) and mid-board vortex (MBV) cores for the angle of attack $\alpha = 24°$, on the leeward (resp. windward) wings. To be consistent with the experiments, the core was identified as the position of maximum longitudinal vorticity. Neither $k-\omega$ SST nor DDES-SST turbulence models are able to maintain the high core velocity plateau shown by the experiments with an overshoot of U varying from about 2.5 to 2.0 along the IBV progression. k-ω SST predicts too low a core axial velocity all along the vortex trajectory, and DDES-SST provides an even lower core axial velocity close to zero from the middle of the wing. On the windward side, the flow reversal occurring in the core of the IBV and MBV vortices shown by the measurements is reasonably well captured by both DDES-SST and $k-\omega$ SST.

There was a general consensus in the NATO/AVT-316 community that the incorrect prediction of the leeward vortex core and its effect on the pressure on the leeward wing leads to an incorrect prediction of the rolling moment and explains the inability of the codes to predict the loss of roll stability. To gain insight, we return to a simpler flow configuration without sideslip effect, the NA1_W1 at 16° angle of attack. This configuration is interesting because we can observe a spectacular difference in the core flow simulation between the k-ω SST RANS and DDES-SST hybrid RANS model, as will be shown in the next section.

5. SYMMETRIC FREE-STREAM CONDITIONS, $\beta = 0°$

5.1 Forces and moments

Fig. 8 shows the drag, lift and pitching moment evolution with respect to the angle of attack α. TUM experiments

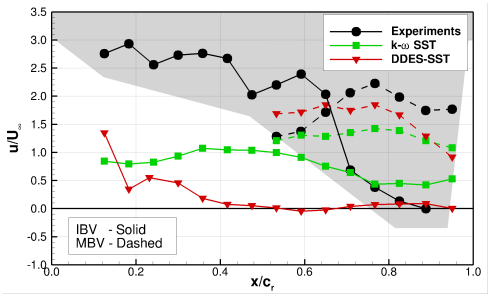

(a) Leeward wing

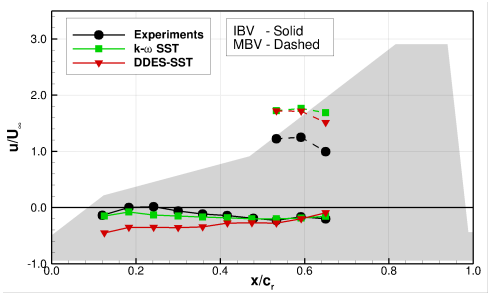

(b) Windward wing

Figure 7: Dimensionless axial velocity for the IBV and MBV for $\alpha = 24°$ and $\beta = 5°$.

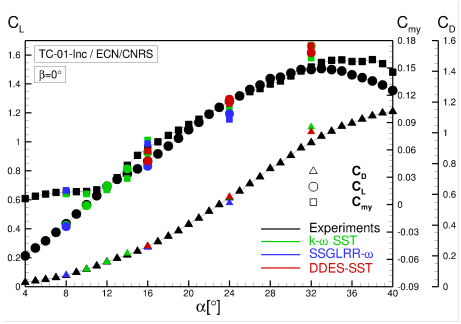

Figure 8: Longitudinal aerodynamic coefficients for $\beta = 0°$ versus α.

are compared to simulations performed with k-ω SST, SSGLRR-ω and DDES-SST turbulence models. Their results are very similar, with a general over-prediction at $\alpha = 32°$.

5.2 α=16°- Global flow characteristics

Fig. 9 presents the vortical structures obtained with the k-ω SST and DDES-SST turbulence models for the angle of attack $\alpha = 16°$. These figures show the isosurface of the dimensionless second invariant, $Q^* = 50$, the blue translucent surface, and the zero-isosurface of the Cartesian axial component of the velocity, the red surface, which in some regions indicates reverse flow. The flow is characterized by two primary leading-edge vortices. The first vortex develops at the most inboard wing

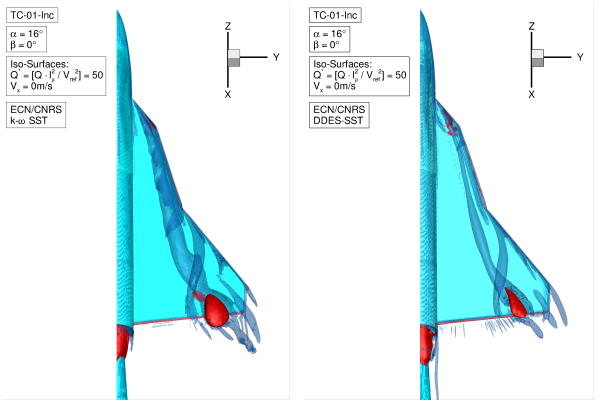

(a) k-ω SST (b) DDES-SST

Figure 9: Time-averaged vortical structures for $\alpha = 16°$ and $\beta = 0°$.

section and is called inboard vortex (IBV). The second vortex develops at the kink from the highly swept to the moderately swept wing section at $x/c_r = 0.475$ and is called mid-board vortex (MBV). All these structures are predicted by every turbulence model. However, their size is thinner with the DDES-SST model, indicating more intense vortices. They have higher peak vorticity and Q values, which the figure does not show.

Fig. 10 shows the surface pressure distribution and skin friction lines for both wings and turbulence closures. NA1_W1 has a lower surface pressure zone on the moderately swept wing region for $k-\omega$ SST which is not present in the DDES-SST simulation, indicating a more intense and stable longitudinal vortex, as expected from a DDES-SST turbulence closure as opposed to most eddy-viscosity models unless they have a strong rotation correction.

Fig. 11 shows the dimensionless axial velocity component at the cross-section x/c_r=0.300 for both wing profiles at an angle of attack $\alpha = 16°$. Results obtained with k-ω SST, SSGLRR-ω, and DDES-SST turbulence closures are compared with TUM experiments at a location specifically chosen to be in the middle of the jet-type plateau. The simulations are not very successful.

Fig. 12 shows the dimensionless axial velocity component at the cross-section x/c_r=0.592, where the TUM experiments indicate a wake-type behaviour for the IBV vortex. Again, this characteristic is not captured by k-ω SST which does not predict the strong decrease of the longitudinal velocity, while DDES-SST provides a very accurate solution which captures this characteristic abrupt evolution in the core of the main vortex. It implicates strong inviscid phenomena, controlled by weaker turbulence effects; this appears to be what makes it so challenging. The MBV vortex is also more intense with DDES-SST and in better agreement with TUM experiments.

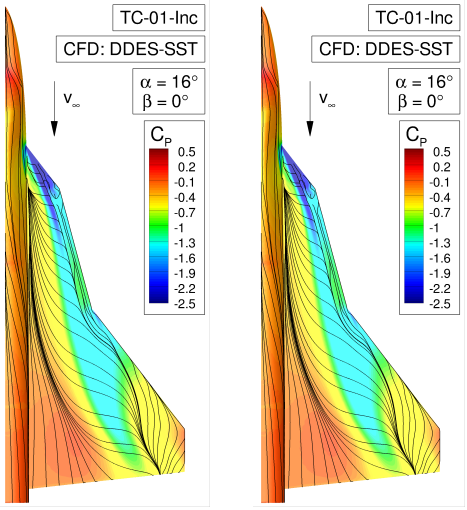

(a) k-ω SST (b) DDES-SST

Figure 10: Surface pressure distribution and skin friction lines for $\alpha = 16°$ and $\beta = 0°$

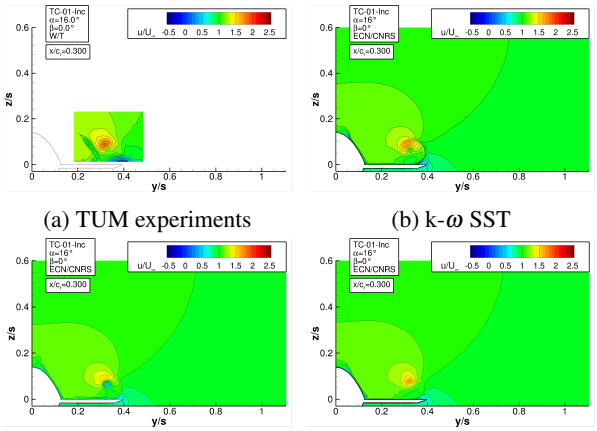

(a) TUM experiments (b) k-ω SST

(c) SSGLRR-ω (d) DDES-SST

Figure 11: Axial component of the velocity at $x/c_r = 0.300$ at $\alpha = 16°$ and $\beta = 0°$

5.3 α=16°- Cross-sections: velocity, core flow extraction, local comparisons close to the onset of reversal

Fig. 13 shows the dimensionless axial velocity, u/U_∞, extracted at the cores of the inboard (IBV) and mid-board (MBV) vortices for the angle of attack $\alpha = 16°$. As mentioned previously, in the experiments, the vortex core in the IBV first exhibits a jet-type core flow with $u/U_\infty \simeq 2$. After $x/c_r \simeq 0.36$, the axial velocity decreases continuously until it reaches 0.1 at $x/c_r \simeq 0.65$. Then the velocity increases slowly as it approaches the trailing edge of the wing. This flow change from a jet-type core to a wake-type core flow is well predicted by the DDES-SST turbulence model while both k-ω SST and SSGLRR-ω fail

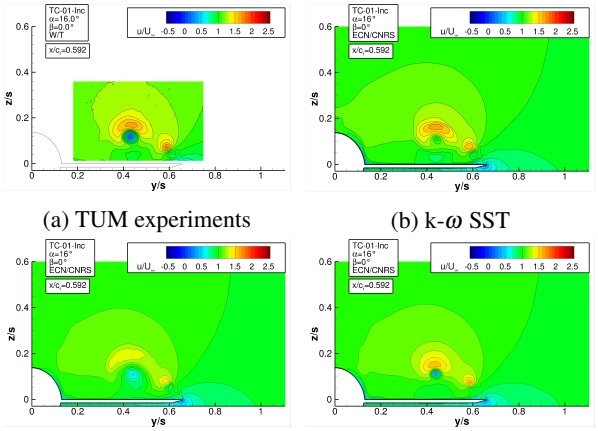

(a) TUM experiments

(b) k-ω SST

(c) SSGLRR-ω

(d) DDES-SST

Figure 12: Axial component of the velocity at x/c_r = 0.592 at $\alpha = 16°$ and $\beta = 0°$

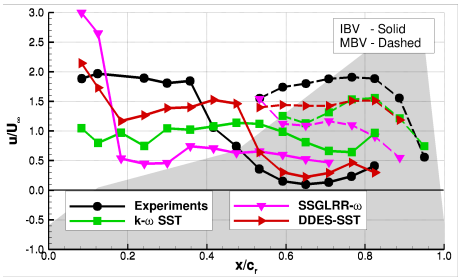

Figure 13: Dimensionless axial velocity for IBV and MBV for $\alpha = 16°$ and $\beta = 0°$.

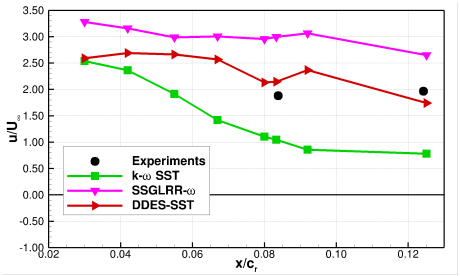

Figure 14: Dimensionless axial velocity at the onset of IBV for $\alpha = 16°$ and $\beta = 0°$.

to predict the jet-type velocity plateau. However, Fig. 14 shows that, close to the onset of the IBV vortex, DDES-SST (in very good agreement with the experiments) and SSGLRR-ω (which over-predicts the core longitudinal velocity) are able to capture a jet-type core configurations contrary to the k-ω SST model which cannot sustain the high longitudinal velocity. We will come back later in the paper to this striking difference and will try to provide an explanation.

5.4 α=16°- Second-moment analysis

In order to compare more thoroughly the physical models, Figs. 15 to 17 show the normal components of the total (i.e. modeled + resolved) Reynolds stress tensor computed by k-ω SST and DDES-SST. For the sake of conciseness, one shows here a comparison at the station x/c_r = 0.3417 in the middle of the longitudinal velocity plateau, where the IBV vortex is considered as mature, being far enough away from its onset but still before its interaction with the second MBV vortex. While $\overline{u'u'}$ is more or less similar for both turbulence models, the transverse components $\overline{v'v'}$ and $\overline{w'w'}$ are very different, the hybrid RANS/LES model showing high values of the total normal second moments in the core of the vortex, as in the shear layer emanating from the leading edge of the triangular wing. This illustrates the higher level of total turbulent kinetic energy present in the core of the vortex, when predicted by DDES.

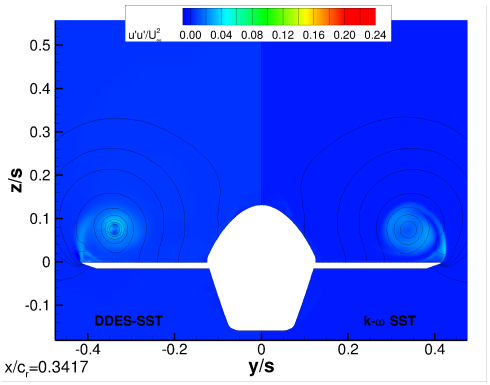

Figure 15: $\overline{u'u'}$ distribution and pressure isolines at x/c_r = 0.3417 for $\alpha = 16°$ and $\beta = 0°$.

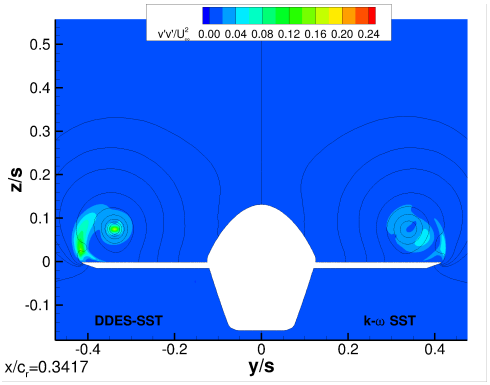

Figure 16: $\overline{v'v'}$ distribution and pressure isolines at x/c_r = 0.3417 for $\alpha = 16°$ and $\beta = 0°$.

The comparison on the $\overline{v'w'}$, see Fig. 18, component reveals striking differences, as well. For the k-ω solution, the core is almost deprived of any transversal shear Reynolds stress which is instead present in the periph-

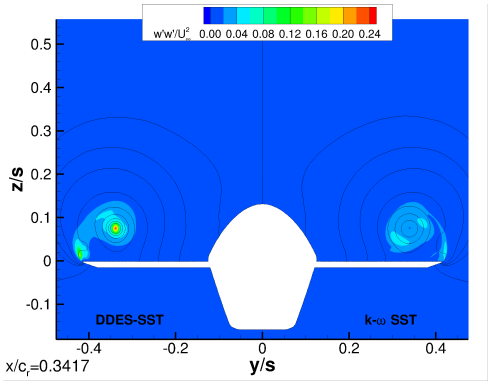

Figure 17: $\overline{w'w'}$ distribution and pressure isolines at x/c$_r$ = 0.3417 for $\alpha = 16°$ and $\beta = 0°$.

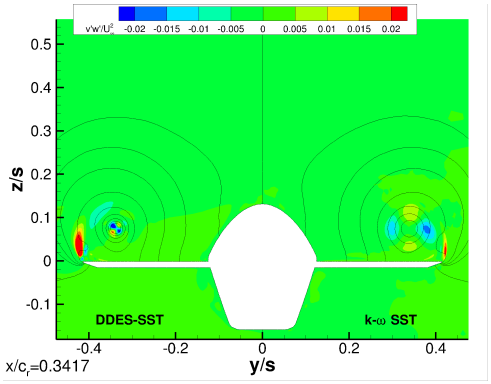

Figure 18: $\overline{v'w'}$ distribution and pressure isolines at x/c$_r$ = 0.3417 for $\alpha = 16°$ and $\beta = 0°$.

ery of the longitudinal vortex and this with a wrong cross distribution aligned with the S_{23} component of the rate-of-strain tensor. In agreement with the normal stress distribution, the hybrid RANS/LES model provides a distribution of the shear Reynolds stress concentrated in the core of the vortex, with the correct Saint-Andrew cross orientation ([3]). This is in strong contradiction with the Boussinesq approximation, and thus out of reach of Linear Eddy-Viscosity Models (LEVM).

The accumulation of large transverse velocity fluctuations in the core of the vortex is due to the interaction of the unsteady transverse vortical ribs-like structures (see Fig. 19 which shows the instantaneous iso surface Q*=50) which are created at the leading edge of triangular wings. They are surrounding the inner core of the IBV vortex and convey, in this core, unsteady content from the outside which contributes to enhance the turbulent kinetic energy. This tke-feeding phenomenon powered by external fluid cannot be captured by the URANS k-ω SST model which is too diffusive to let these unsteady transversal structures develop.

In order to understand the physical mechanisms at play, Fig. 20a shows instantaneous iso-Q surfaces and their

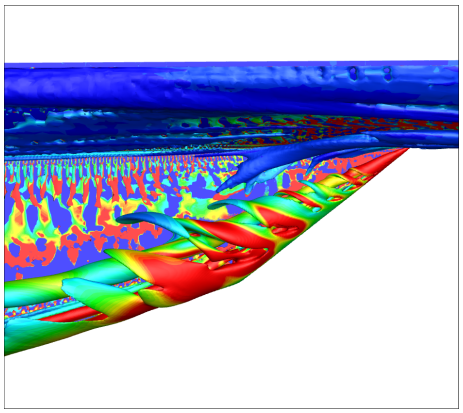

Figure 19: Iso-Q*=50 distribution for $\alpha = 16°$ and $\beta = 0°$.

cross-section at x/c$_r$ = 0.080. One can clearly see that the vortical tube which is surrounded by a stable and relatively steady shear layer, although we cannot rule out the possibility that finer grids would support small-scale turbulence. Fig. 20b shows a cross-section located further downwind at x/c$_r$ = 0.132, at the beginning of the second triangular wing. One can notice that the shear layer is now no more steady and is divided into several unsteady transverse vortices which excite the core vortex and penetrate its periphery. A second longitudinal vortex located between the oblique leading edge and the main IBV vortex is also visible to attentive eyes. Then, Fig. 20c (resp. Fig. 20d) shows a view of the flow in the first (resp. central) part of the second triangular wing at x/c$_r$ = 0.132 (resp. x/c$_r$ = 0.180). The phenomenon previously described is amplified with more unsteady transverse structures and a stronger impact in the core of the IBV vortex. The figures illustrate the rich content of resolved turbulence.

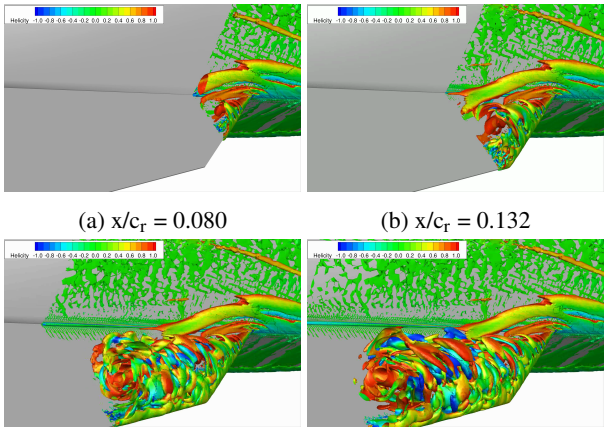

(a) x/c$_r$ = 0.080 (b) x/c$_r$ = 0.132

(c) x/c$_r$ = 0.180 (d) x/c$_r$ = 0.219

Figure 20: $\beta = 0°$ $\alpha = 16°$ - DDES-SST - Transversal views of the instantaneous iso-Q surfaces colored by helicity at various cross-sections.

6. AN ATTEMPT AT THE ANALYSIS OF THE TURBULENCE CHARACTERISTICS IN THE CORE

6.1 TKE budget analysis

A procedure for calculating the turbulence kinetic energy (tke) budget has been recently implemented in ISIS-CFD, utilizing the discretized form of the momentum equations resolved with the hybrid RANS/LES formulation.

$$\begin{aligned} \overline{u_i'\left(\frac{\partial \rho u_i}{\partial t} + R(u_i, \overrightarrow{u}, p, \mu, \mu_t)\right)} &= \frac{\partial \rho \bar{k}}{\partial t} + A - P \\ &- D^u - D^p \\ &- D^k_{dns} + \varepsilon_{dns} \\ &- D^k_{mod} + \varepsilon_{mod} \end{aligned} \quad (1)$$

where R stands for the RANS operator. If the unsteady momentum residuals are enough converged at each time step, the left-hand side term should be close to zero, which guarantees the discrete equilibrium of the tke budget. However, it is expensive to reduce these non-linear residuals enough to achieve a perfect equilibrium and work is on-going on this topic to improve the tke budget balance for industrial applications. Nevertheless, based on this algorithm, we can evaluate the various source terms which control the spatial distribution of tke.

Fig. 21 shows the correlations associated with the non-linear convection terms, i.e. the advection $A = \frac{\partial}{\partial x_k}(\rho \overline{u_k} k)$, the production $P = -\rho \overline{u_i' u_k'} \frac{\partial \overline{u_i}}{\partial x_k}$, the turbulent diffusion $D^u = -\frac{\partial}{\partial x_k}\left(\frac{\rho}{2}\overline{u_k' u_i' u_i'}\right)$ and the pressure-velocity diffusion $D^p = -\frac{\partial}{\partial x_k}\left(\overline{p' u_k'}\right)$. The station x/c_r = 0.3417 is shown.

At this specific location but also for the stations located farther upwind, the main zone of production of tke occurs in the shear layer created at the leading edge of the triangular wing. In the core of the vortex, one also notices a four-leaf clover pattern with successive negative and positive production regions; this is also ruled out by the Boussinesq assumption. Apart from this core, the production is smaller in the main part of the vortex. The advection, pressure and turbulent diffusion terms exhibit a very similar distribution in the core of the vortex and negative and positive advection regions alternate in the leading edge shear layer. It is striking to notice that none of these source terms is individually axisymmetric in the core of the vortex while their sum is, as it should be since tke is close to axisymmetric in the core; recall however that the (x, y, z) axes are not quite aligned with the axis of the vortex. The four remaining source terms are the viscous and modeled diffusion and dissipation which are shown in Figs 22, the modeled dissipation having to be reconstructed for a hybrid RANS/LES turbulence model

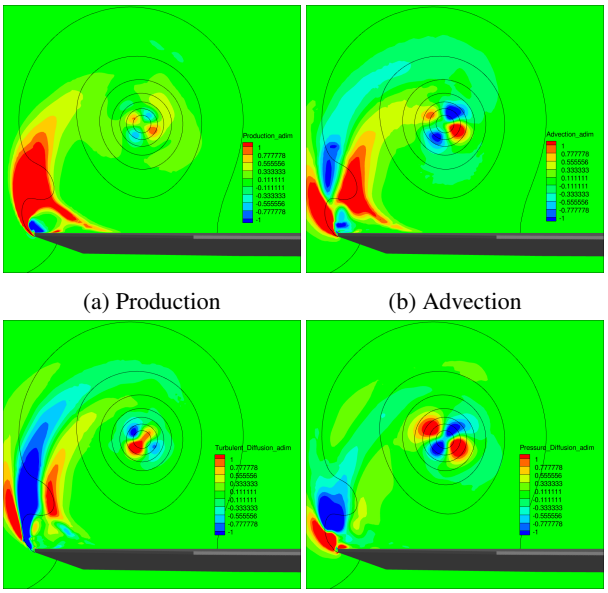

(a) Production (b) Advection

(c) Turbulent diffusion (d) Pressure Diffusion

Figure 21: $\beta = 0°$ $\alpha = 16°$ - DDES-SST - Production, advection, pressure and turbulent diffusion terms of the tke budget at $x/c_r = 0.3417$.

contrary to a pure LES tke budget. As expected, these remaining terms are axisymmetric in the vortex with a maximum occurring at its center; this could be due to them being far less dependent on the axes than the previ-

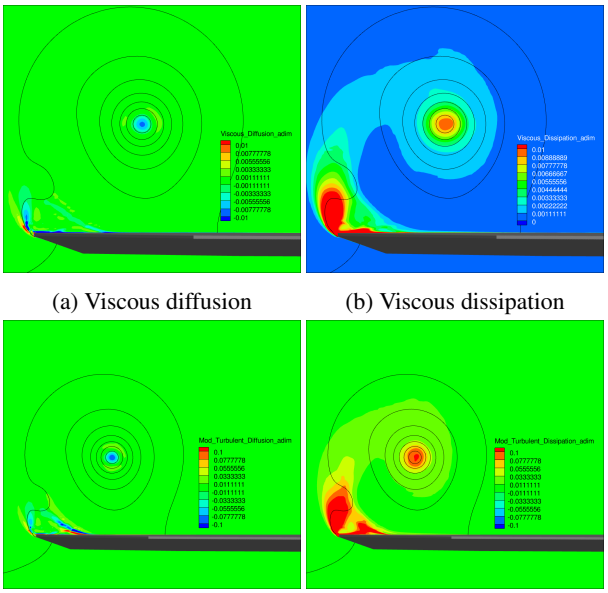

(a) Viscous diffusion (b) Viscous dissipation

(c) Modeled turbulent diffusion (d) Modeled turbulent dissipation

Figure 22: $\beta = 0°$ $\alpha = 16°$ - DDES-SST - Viscous and modeled diffusion and dissipation terms of the tke budget at $x/c_r = 0.3417$.

ous terms. The diffusion term is about ten times smaller than the dissipation, whether viscous or modeled. Although the mesh is locally refined, it is obviously not fine enough to capture the small scales responsible for the viscous diffusion/dissipation effects, the way it would happen in a DNS. The modeled turbulent diffusion and dissipation terms are significantly larger (about ten times) than their viscous counterparts. Accounting for the dissipation by the sub-grid-scale (SGS) model is an essential part of LES or DES interpretations.

6.2 Comparing DDES with SSGLRR-ω in URANS mode

Because of the high level of turbulent eddy-viscosity in the vortex, the k-ω SST model provides a steady and stable solution even when the computations are run in unsteady mode, which is a reasonable behavior. In contrast with the k-ω SST model, the SSGLRR-ω RSTM model which is deprived of any explicit turbulent viscosity is more prone to unsteady destabilisation. We have therefore run a SSGLRR-ω computation in unsteady mode with the same time step as the one used for the hybrid RANS/LES simulations. Fig. 23 shows a comparison between the instantaneous iso-Q=50 surfaces computed with both models. First of all, one can notice that the SSGLRR-ω model captures the destabilisation of the shear layer emanating from the leading edge of triangular wings and can generate the transverse vortical structures surrounding the main IBV vortex, which is very encouraging at first glance. A closer look reveals that the content in transverse vortical structures is less rich in the SSGLRR-ω simulation, particularly in the onset region in the first triangular wing where no strong-enough destabilization of the shear layer takes place in the SSGLRR-ω computation. The RANS eddy viscosity is larger than the DDES eddy viscosity.

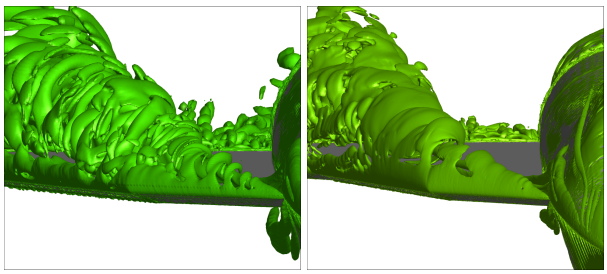

(a) DDES-SST (b) SSGLRR-ω

Figure 23: $\beta = 0^\circ$ $\alpha = 16^\circ$ - Instantaneous iso-Q=50 isosurfaces.

Fig. 24 (resp. 25) shows a comparison of pressure isolines and total (i.e. modeled + resolved) $\overline{u'u'}$ and $\overline{v'v'}$ (resp. $\overline{w'w'}$ and $\overline{v'w'}$) second moments for different turbulence closures at the same location as previously, namely $x/c_r = 0.3417$. The DDES solution for the Reynolds stress tensor is characterized by transverse normal components which are similar in magnitude and larger than the streamwise normal component. On the contrary, the SSGLRR-ω solution is characterized by strong streamwise Reynolds stress (about two times stronger than its DDES counterpart) and two transverse normal Reynolds stresses which are similar in magnitude but of which the maximum is off-center with respect to the center of the vortex, contrary to the DDES solution. The shear Reynolds stress $\overline{v'w'}$ is about two times weaker with DDES than with SSGLRR-ω, and although the Saint Andrew cross configuration is captured by both turbulence closures, the negative and positive branches are inverted, which suggests that they may not be physical.

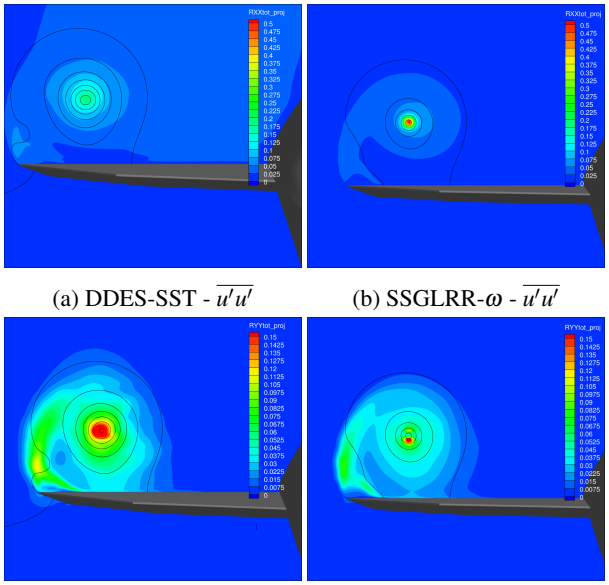

(a) DDES-SST - $\overline{u'u'}$ (b) SSGLRR-ω - $\overline{u'u'}$

(c) DDES-SST - $\overline{v'v'}$ (d) SSGLRR-ω - $\overline{v'v'}$

Figure 24: $\beta = 0^\circ$ $\alpha = 16^\circ$ - $\overline{u'u'}$ and $\overline{v'v'}$ computed by DDES and SSGLRR-ω at $x/c_r = 0.3417$.

Finally, Fig. 26 shows a fair agreement for the total turbulent kinetic energy computed by both turbulence models. Apart from the core for which the maximum value of tke is almost identical for both models, one notices that the hybrid RANS/LES model produces slightly more turbulent kinetic energy in the vortex and in the shear layer shed at the leading edge. This is related to the poorer content in scales observed on the iso-Q surface presented previously (see Fig. 23).

6.3 IBV onset analysis

Because of the use of a powerful anisotropic mesh adaptation, it is possible to put enough points at the onset of the IBV vortex and perform a comparison of the turbulence models to explain the trend previously observed in

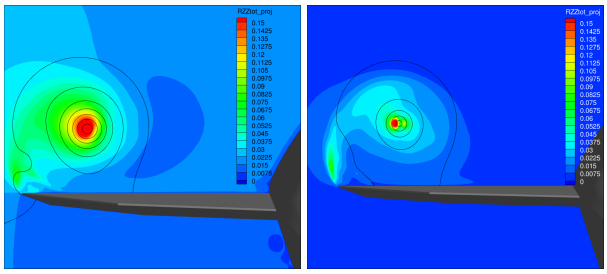

(a) DDES-SST - $\overline{w'w'}$ (b) SSGLRR-ω - $\overline{w'w'}$

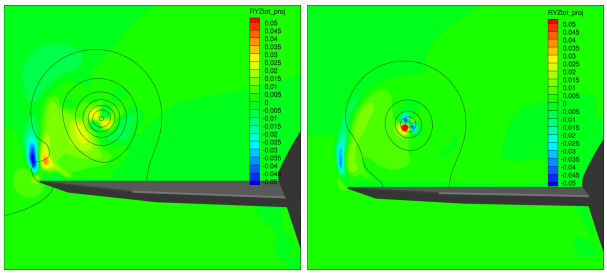

(c) DDES-SST - $\overline{v'w'}$ (d) SSGLRR-ω - $\overline{v'w'}$

Figure 25: $\beta = 0°$ $\alpha = 16°$ - $\overline{w'w'}$ and $\overline{v'w'}$ computed by DDES and SSGLRR-ω at $x/c_r = 0.3417$.

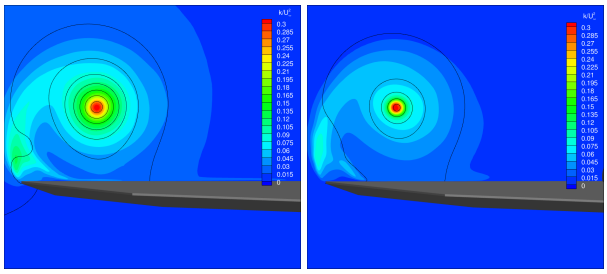

(a) DDES-SST (b) SSGLRR-ω

Figure 26: $\beta = 0°$ $\alpha = 16°$ - Total turbulent kinetic energy computed by DDES and SSGLRR-ω at $x/c_r = 0.3417$.

Fig. 14. A comparison of the tke production at $x/c_r = 0.0175$ is shown in Fig. 27. One can observe that DDES-SST predicts a flow with a limited amount of tke production (yellow/green tongue around 25), while the RSTM (resp. k-ω SST) model predicts a red tongue of maximum tke production value of 40 (resp. 130, notice the different color scale for k-ω SST). This is somewhat surprising considering that this region is still not far from a thin shear layer, for which RANS models were all calibrated.

A bit further downwind, at $x/c_r = 0.080$, close to the first experimental point, Fig. 28 shows the same comparison of the tke production computed by different turbulence models. At this location, DDES-SST still predicts a flow with a reduced turbulence production while both models start to predict similar tke production levels. An in-depth analysis of the onset conditions should be performed in the future but one might think that this

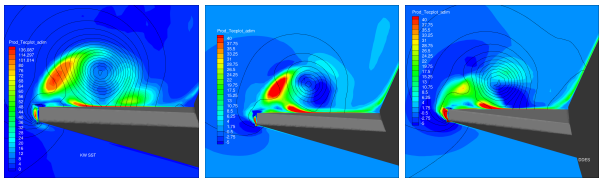

(a) k-ω SST (b) SSGLRR-ω (c) DDES-SST

Figure 27: $\beta = 0°$ $\alpha = 16°$ - Production of total kinetic energy at $x/c_r = 0.0175$.

suggests the possibility of a laminar-to turbulent transition in this region in the experiments which would be, by chance, correctly captured by the hybrid RANS/LES model. This zone of laminarisation would totally change the onset condition and might give rise to and sustain a strong jet-type core velocity distribution. To be complete, recall that the "underlying" RANS model of the DDES is SST, with the same inflow values of k and ω as in the RANS runs, so that the boundary layers should be very similar.

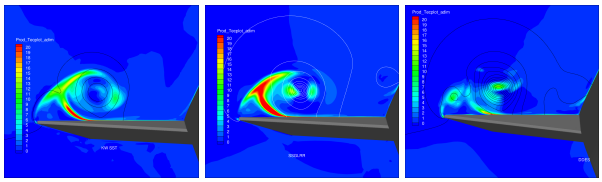

(a) k-ω SST (b) SSGLRR-ω (c) DDES-SST

Figure 28: $\beta = 0°$ $\alpha = 16°$ - Production of total kinetic energy at $x/c_r = 0.080$.

7. CONCLUSIONS AND PERSPECTIVES

Although a simple link between the flow characteristics and the rolling moment instability has not been revealed in this paper, thanks to the joint use of adaptive mesh refinement and hybrid RANS/LES turbulence models, some characteristics of the inner core flow physics which might affect the rolling instability have been exhibited.

- Contrary to RANS models, DDES-SST does not create high production at the onset of the longitudinal vortex at the junction between the wing and the fuselage, which leads to a laminar-like flow in the early development of the vortex. This sets the conditions of strong jet-like characteristics. In strongly-distorted flow fields, basic two-equation RANS models suffer from tke production outside the vortical region, which is physically paradoxical and has long been called (in 2D) the Stagnation-Point Anomaly. The behavior of the RSTM in that region is more complex.

- DDES-SST predicts very different physics in the core of the vortex with a peak of high turbulent kinetic energy created by the high velocity fluctuations coming from the unsteady transverse vortical structures emanating from the oblique leading edges.
- Although an RSTM model run in unsteady mode appears promising at first glance, the turbulence anisotropy in the vortex core is quite different from the DDES-SST prediction and looks dubious.
- The tke budget analysis illustrates the deep modifications which should be included in modeled source terms to take into account the physics simulated by DDES-SST. However, the present formulation has to be improved to be less sensitive to the level of reduction of the unsteady momentum residuals.

Future studies will include mesh refinement with systematic threshold reduction. In a DES or an LES for that matter, on a finer grid, the sub-grid-scale (SGS) dissipation is the product of a smaller SGS viscosity (nominally, proportional to $\Delta^{4/3}$) and larger strain rates, and it is vital to check how this trade takes place and the two compensate. The SGS contribution normally dominates over the molecular one, as we found.
We intend to develop a general strategy for grid design and adaptation in hybrid simulations. This is a great current challenge, and meeting it with goal-oriented criteria would be a considerable achievement.
An ultimate goal is a convincingly better RANS model. The propagation of fresh knowledge in turbulence physics to such a model is a slow process. Hybrid methods will be in very wide use for at least this decade and the next, so that RANS models and especially their prediction of smooth-body separation will remain major areas of study.

8. ACKNOWLEDGMENT

We would like to thank Airbus Defence and Space GmbH for providing the generic A/C configuration and the experimental data, and for authorizing the publication of the presented results. The computations were performed using HPC resources from GENCI (Grand Equipement National de Calcul Intensif) (Grant-A0082A00129, Grant-A0102A00129, Grant-A0122A00129) which is gratefully acknowledged.

REFERENCES

[1] F. Alauzet and A. Loseille. High-order sonic boom modeling based on adaptive methods. *Journal of Computational Physics*, 229(3):561–593, 2010.

[2] R.-D. Cécora, R. Radespiel, B. Eisfeld, and A. Probst. Differential reynolds-stress modeling for aeronautics. *AIAA Journal*, 53(3):1–17, 2015. Published online: 10 September 2014, March 2015.

[3] J. Chow, G. Zilliac, and P. Bradshaw. Turbulence measurements in the near field of a wingtip vortex. *NASA-Technical Memorandum*, 110418, 1997.

[4] G. B. Deng and M. Visonneau. Comparison of explicit algebraic stress models and second-order turbulence closures for steady flows around ships. In *In 7th International Conference on Numerical Ship Hydrodynamics*, 1999.

[5] R. Duvigneau and M. Visonneau. On the role played by turbulence closures in hull shape optimization at model and full scale. *J. Mar. Sci. Technol.*, 8:11–25, 2003.

[6] P. L. George, F. Hecht, and M. G. Vallet. Creation of internal points in Voronoi's type method. Control adaptation. *Advances in Engineering Software*, 13(5/6):303–312, 1991.

[7] E. Guilmineau, G. Deng, A. Leroyer, P. Queutey, M. Visonneau, and J. Wackers. Assessment of hybrid RANS-LES formulations for flow simulation around the Ahmed body. *Computers & Fluids*, 176:302–319, 2015.

[8] S. M. Hitzel, A. Winkler, and A. Hövelmann. Vortex Flow Aerodynamic Challenges in the Design Space for Future Fighter Aircraft. In A. Dillman, G. Heller, E. Krämer, C. Wagner, C. Tropea, and S. Jakirlic, editors, *Notes on Numerical Fluid Mechanics and Multidisciplinary Design*, volume 142 of *New results in Numerical and Experimental Fluid Mechanics XII. DGLR 2018.*, pages 297–306. Springer, 2020.

[9] S. Mozaffari, E. Guilmineau, M. Visonneau, and J. Wackers. Average-based mesh adaptation for hybrid RANS/LES simulation of complex flows. *Computers & Fluids*, 232:105202, 2022.

[10] S. Pfnür and C. Breitsamter. Leading-Edge Vortex Interactions at a Generic Multiple Swept-Wing Aircraft. *Journal of Aircraft*, 56(6):2093–2107, 2019.

[11] M. Visonneau, E. Guilmineau, and G. Rubino. Local flow around a surface combatant at various static drift conditions: The role played by turbulence closures. In *33rd Symposium on Naval Hydrodynamics*, Osaka, Japan, 2020.

[12] J. Wackers, G. B. Deng, E. Guilmineau, A. Leroyer, P. Queutey, and M. Visonneau. Combined refinement criteria for anisotropic grid refinement in free-surface flow simulation. *Computers & Fluids*, 92:209–222, 2014.